Barrier tunneling and loop polarization in Hopf semimetals

Ji-Huan Guan,[1,2] Yan-Yang Zhang,[3,4,*] Si-Si Wang,[1,5] Yan Yu,[1,2] Yang Xia,[6,7] and Shu-Shen Li[1,5,8]

[1]*SKLSM, Institute of Semiconductors, Chinese Academy of Sciences, P.O. Box 912, Beijing 100083, China*

[2]*School of Physical Sciences, University of Chinese Academy of Sciences, Beijing 100049, China*

[3]*School of Physics and Materials Science, Guangzhou University, 510006 Guangzhou, China*

[4]*Research Center for Advanced Information Materials, Guangzhou University, 510006 Guangzhou, China*

[5]*College of Materials Science and Opto-Electronic Technology, University of Chinese Academy of Sciences, Beijing 100049, China*

[6]*Microelectronic Instrument and Equipment Research Center, Institute of Microelectronics of Chinese Academy of Sciences, Beijing 100029, China*

[7]*School of Microelectronics, University of Chinese Academy of Sciences, Beijing 100049, China*

[8]*Synergetic Innovation Center of Quantum Information and Quantum Physics, University of Science and Technology of China, Hefei, Anhui 230026, China*

(Received 8 April 2020; revised 19 June 2020; accepted 28 July 2020; published 7 August 2020)

Degrees of freedom like charge, spin, and valley in condensed matter have drawn much attention in the past decades. Recently, several kinds of nodal line semimetals have been discovered for which the conduction and valence bands cross along one-dimensional lines, usually forming loops. These distinct loops, similar to valleys, can be used as a possible carrier of information. Here we investigate the loop polarization during quantum transports, i.e., barrier tunneling as well as disorder scattering, in Hopf semimetals with two disconnected loops. We find that in both cases, the loop polarization is mostly dominated by the performance of normal incidence, due to the mirror symmetry of two loop planes and the finite size effect along one direction. After scattered by nonmagnetic disordered potentials, the opposite polarizations can intrinsically reveal the topological structure of two loops, linked or unlinked. The effects from smooth barriers and disorders are also investigated. We find that a long range smooth barrier leads to an even clearer and purer picture of scattering and loop polarization, due to the suppression of large momentum transfer. These effects can be used as a controllable loop filter and detector.

DOI: 10.1103/PhysRevB.102.064203

I. INTRODUCTION

Valley degree of freedom widely exists in various materials, such as graphene [1–6], silicon [7], and transition-metal dichalcogenide (TMD) monolayer [8–12], which has become an attractive subject known as "valleytronics." The valley states residing at the minima of bands are well separated from each other in momentum space and can be manipulated as an independent physical quantity similar to electronic charge and spin. Recently, nodal line semimetals have been proposed in several models and materials [13,14]. In contrast to nodal point semimetals (Weyl or Dirac semimetals), the conduction and valence bands in nodal line semimetals are intersected along a one-dimensional (1D) line, instead of a point. In many cases, the line is end-to-end self connected, forming a closed nodal loop in the momentum space. The loops in nodal line semimetals possess rich geometric and topological structures [15–30].

If there are more than one loops present, they can form rich configurations in the three-dimensional (3D) momentum space. Among them, the typical "two-loop" systems are dubbed Hopf semimetals or nodal link semimetals [15–21], where the two nodal loops are linked but disconnected, as shown in Fig. 1(a). This provides two distinguishable states for electrons to stay, one loop or the other. Furthermore, nodal chain [22–24], nodal net [25,26], nodal knot [27,28], and other multiloop [19,29] semimetals have also been proposed or even realized in experiments. These nodal line systems are usually protected by mirror symmetry [17,30], $\mathcal{PT}$ symmetry (the combination of inversion symmetry and time-reversal symmetry) [16,18], or other crystallographic symmetries [22,29]. Candidate materials that host the Hopf links include Co_2MnGa [17], MgSrSi-type crystals [29], Ba_3Si_4 [22], etc.

For an application of the loop degree of freedom, the polarization is the primary concern. In previous researches in valleytronics, the valley polarization can be realized by quantum point contact [1], line defect [4,31], pseudospin-assisted tunneling [32], nonmagnetic disorder [8], Dirac gap [3], spin-orbit coupling [10], orbital magnetic moment [2], Berry curvature [6], gate voltage [5] or optical pumping [9,11,12], etc. In this paper, we numerically investigate the polarization of loops in Hopf semimetals by simulating quantum transports through a potential barrier or a disordered region, respectively. We find that the loop polarization can be well understood from the performance of normal incidence which respects the pseudospin conservation. Inspired by the research on TMDs [8], we also propose a disorder induced loop polarization, which

*yanyang@gzhu.edu.cn

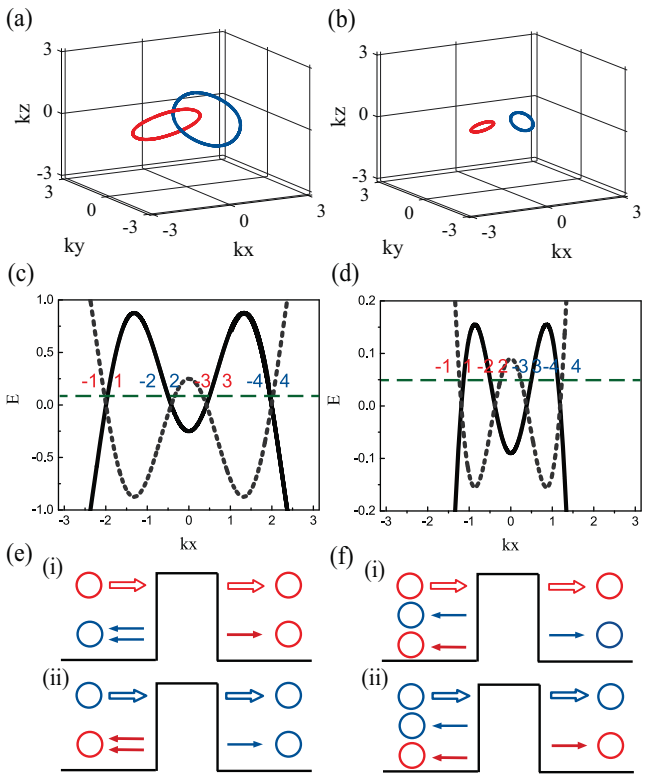

FIG. 1. The left (right) column corresponds to the linked (unlinked) case. (a),(b) Two loops in momentum space at zero energy for $m_0 = 2.5$ (linked) and $m_0 = 3.3$ (unlinked), respectively. (c),(d) Band structures for $k_y = 0$ and $k_z = 0$ with the same parameters as (a) and (b), respectively. Solid and dashed bands carry opposite pseudospins. The horizontal green line presents the Fermi energy, crossing the bands at states '$-1, 1, -2, 2, -3, 3, -4, 4$' in sequence, where red/blue numbers denote the channels on red/blue loop. (e),(f) Illustration of scattering processes. The red/blue loop denotes the channels on red/blue loop, and the hollow arrows are for incident channels. (i) and (ii) in (e) and (f) represent the scattering of incident electronic states on the red loop and the blue loop, respectively.

is an intrinsic nature embedded in momentum space and does not rely on much details of specific materials. The topology of linked or unlinked can be distinguished from the opposite directions of disorder-induced polarization.

The paper is organized as follows. In the next section, we introduce the two-band model of Hopf semimetals. In Sec. III, barrier tunneling is considered, including the momentum resolved scattering in the x direction and the scattering with finite width N_z. Besides, quantum transport along other axes is also discussed. In Sec. IV, the disorder induced polarization is investigated. The effects of smooth potential barrier and disorder are given in Sec. V. Section VI is a summary. The computational method and the detailed scattering amplitudes of barrier tunneling at normal incidence are provided in the Appendix.

II. THE MODEL

The concrete realization of a Hopf loop model depends on the symmetry. For example, the Hopf loops protected by the mirror symmetry require at least four bands and the coupling between two loops can be artificially tuned from zero to strong, which is determined by an off-diagonal submatrix [17]. In this paper, we adopt the simplest two-band Hopf semimetal model [16], where loops are protected by $\mathcal{PT}$ symmetry. This generic model is derived from a general method based on Hopf maps [33], and the tight-binding model can be realized on a 3D cubic lattice with two orbitals at each site as

$$H(\boldsymbol{k}) = \mathcal{A}\tau_x + \mathcal{B}\tau_z, \tag{1}$$

where

$$\mathcal{A} = 2\sin k_x \sin k_z + 2\sin k_y \left(\sum_{i=x,y,z} \cos k_i - m_0\right),$$

$$\mathcal{B} = \sin^2 k_x + \sin^2 k_y - \sin^2 k_z - \left(\sum_{i=x,y,z} \cos k_i - m_0\right)^2,$$

with τ_x, τ_z Pauli matrices acting on the subspace of pseudospins (sublattices). To simplify the model, we have made m_0 the only tunable model parameter, with appropriate fixing of other parameters. Notice that m_0 also appears in the off-diagonal elements and therefore it determines some hopping integrals in the real space, after an inverse Fourier transformation on the 3D cubic lattice.

When $m_0 \in (1.0, 3.4)$, the energy spectrum of model (1) is always gapless and the band-touching manifolds at energy $E = 0$ form two distinct 1D loops. An interesting transition occurs at the critical point with $m_0 = 3.0$: When $m_0 < 3.0$, two loops are linked [Fig. 1(a)], and otherwise they are unlinked [Fig. 1(b)]. The loop equations can be solved by setting $\mathcal{A} = 0$ and $\mathcal{B} = 0$ simultaneously. One loop is $k_y = k_z$, $\sin k_x = m_0 - \sum_{i=x,y,z} \cos k_i$, and the other is $k_y = -k_z$, $\sin k_x = \sum_{i=x,y,z} \cos k_i - m_0$, as shown in Figs. 1(a) and 1(b). Notice that two loops lie in two planes $k_y = \pm k_z$, respectively. When the Fermi energy slightly deviates from zero energy, the Fermi surface evolves from 1D loops to doughnut surfaces which are closed two-dimensional (2D) manifolds.

III. BARRIER TUNNELING IN HOPF SEMIMETALS

Barrier tunneling is a typical problem in the quantum transport. For example, one of the novelties of Dirac fermions is the Klein tunneling, in which electrons can pass through the barrier without any back-reflection [34]. This phenomenon appears not only in high-energy physics but also in condensed matter, such as graphene [35], Dirac/Weyl semimetals [36], and Dirac loop semimetals [37]. In this paper, we will illustrate that similar physics can be generalized to this two-band Hopf semimetal model.

Here, we consider the electrons injecting through a pseudospin independent square potential barrier $\sigma_0 V(\boldsymbol{x})$, with

$$V(\boldsymbol{x}) = \begin{cases} V_0, & 0 < x < d, \\ 0, & x < 0, x > d, \end{cases} \tag{2}$$

which has finite width d along the x direction and extends infinitely along other directions. Notice that the line

connecting the central points of two Hopf loops is also along the x direction. This setup will be helpful for a fine tuning and investigation of the scattering between two loops. The k_y and k_z are conserved due to the absence of scattering in these directions from this y and z independent barrier (2). Because of these conservations, the calculation of scattering amplitudes can be effectively reduced to a 1D problem with constant k_y and k_z. In the following, the simulations are based on the tight-binding model (1) and the lattice version of mode matching approach [38,39], by which channel resolved scattering amplitudes can be numerically obtained. This method relies on a Green's function formalism and the details are presented in Appendix.

The focus of this paper is the polarization of two distinct loops during scattering, in the low energy regime, i.e., Fermi energies around the band-touching loops. In order to quantitatively characterize this problem, we define the net loop transmission (NLT) as

$$T_{\text{net}} = T_{\text{red}} - T_{\text{blue}}, \tag{3}$$

where T_{red} (T_{blue}) denotes the total transmission amplitude of scattering *into* the red (blue) loop region. The colors "red" and "blue" are just names to label two distinct loops as illustrated in Figs. 1(a) and 1(b). Here, T_{net}, as well as T_{red} and T_{blue}, can be defined to a specific incident state (k_x, k_y, k_z), or to a group of incident states at the same Fermi surface, which are just a simple summation over these states. Correspondingly, the loop polarization rate is defined as

$$P = T_{\text{net}}/(T_{\text{red}} + T_{\text{blue}}), \tag{4}$$

along with the conductance (in units of $\frac{e^2}{h}$)

$$G = T_{\text{red}} + T_{\text{blue}}. \tag{5}$$

A quantum transport from an injecting state is loop polarized as long as T_{net} or P is nonzero. The zero temperature conductance is an integration of transmissions over all injecting states on the Fermi surface, and the total NLT associated with the Fermi surface can be defined similarly.

The model system (1) we investigate is a 3D system, which is infinite in three directions. Since the barrier (2) respects the translation invariant in y and z directions, mathematically this system can be treated as an effectively 1D problem with momenta k_y and k_z as parameters, but the physics is still three dimensional.

Firstly, we consider the normal incidence of electronic tunneling where $k_y = 0$ and $k_z = 0$. In Figs. 1(c) and 1(d), we illustrate the 1D band structures at $k_y = k_z = 0$ for the linked and unlinked cases, respectively. Four band crossing points labeled with blue (red) numbers belong to the blue (red) loop, respectively, with the sign $\pm$ indicating the direction of its group velocity. In this case, $\mathcal{A}$ in Hamiltonian (1) equals to zero and the Hamiltonian is written as

$$H(\mathbf{k}) = \mathcal{B}\tau_z,$$

whose eigenstates possess well-defined pseudospin eigenvalues $\tau_z = 1$ or $\tau_z = -1$, which are plotted in Figs. 1(c) and 1(d) as solid and dashed lines, respectively. In the tunneling process through the barrier (2), the pseudospins of electrons are conserved, resembling the normal incidence of Dirac electrons in graphene [35]. Electrons with one pseudospin are forbidden to scatter into states with the opposite pseudospin. For example, in the linked case [Fig. 1(c)], the incident state '1' of the red loop in the solid line band can only be transmitted into states '1' or '3' on the same loop or be reflected back to states '−2' and '−4' on the other loop, whereas other processes are not allowed. Also notice that in the linked case, states '−1, 1, −3, 3' belong to red loop while '−2, 2, −4, 4' belong to blue loop. Similar discussions can be done in the unlinked case. The details of scattering amplitudes for each channel at normal incidence are presented in Appendix.

These scattering processes of normal incidence can be summarized in Figs. 1(e) and 1(f). Figure 1(e) illustrates the above mentioned scattering of injecting electronic states on the red loop (i) or the blue loop (ii), in the case of linked loops. For example, in Figs. 1(e) and 1(i), an injecting electron on the red loop can be transmitted to the same state (hollow arrow) or another state (solid arrow) on the red loop. On the other hand, it can be reflected back to either of the states on the blue loop (two solid arrows). Other scattering processes are forbidden. As for the unlinked case, Fig. 1(f) depicts the scattering of injecting electrons on the red loop (i) or the blue loop (ii). In Figs. 1(f) and 1(i), an injecting electron on the red loop can be transmitted to the same state on the loop (hollow arrow) or a state on the blue loop (solid arrow). Its reflection can also be scattered to either of the states on red and blue loops (two solid arrows).

The above simple pictures are only for the low energy region around the band-touching loops. In a tight-binding model, they will be changed somehow by the band structure at higher energies. For instance, in Fig. 1(c), the solid line band carrying states '1,' '−2,' '3,' and '−4' will terminate at $E \sim 0.9$, and the dashed line band carrying states '2' and '−3' will terminate at $E \sim 0.2$. These energy cutoffs will manifest themselves in the following tunneling processes.

Numerical results of barrier tunneling from a normal incidence as functions of the barrier height V_0 are shown in Fig. 2, where the left column (a), (c), (e) is for the linked case with $m_0 = 2.5$, and the right column (b), (d), (f) is for the unlinked case with $m_0 = 3.3$. First let us understand the results presented in Fig. 2(a), with a comparison to Fig. 1. Starting from $V_0 = 0$, both injecting channels on both loops, i.e., channels 1 and 3 in the red loop and channels 2 and 4 in the blue loop, can be almost perfectly transmitted, giving rise to $T \sim 2$ associated with both loops. Increasing V_0 will introduce scattering. Notice that the energy profile in the barrier is lifted by V_0, and therefore what the injecting electron with $E = 0.05$ sees in this region is the band structure at $E^{\pm} - V_0$. Therefore, when $V_0 \sim 0.25$, the local minimum around $k_x = 0$ of the solid line band (where channel 3 of the red loop resides) will be shifted to the Fermi energy of the injecting electron. After that, this channel will be evanescent in the barrier region. This explains the sudden drop of T_{red} from ∼2 to ∼1 around $V_0 \sim 0.25$ in Fig. 2(a). The vanishing of T_{blue} at $V_0 \sim 0.9$ can be similarly understood, where the dashed line band carrying channels 2 and 4 disappears at the Fermi energy. This furthermore leads to a 100% loop polarization shown in Fig. 2(e). Since the backscattering is not prohibited (here to opposite loops), the transmissions are not perfect, and sometimes exhibit resonance oscillations from

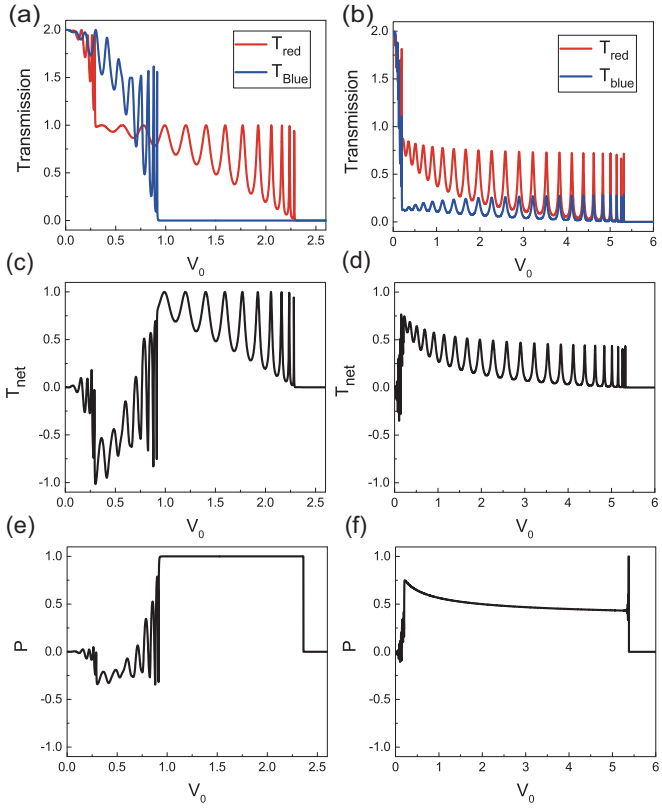

FIG. 2. Transmissions as functions of barrier height V_0, with $m_0 = 2.5$ (left column, linked case) and $m_0 = 3.3$ (right column, unlinked case). (a),(b) Transmission amplitudes of electronic scattering into red (T_{red}) and blue (T_{blue}) loops. (c),(d) NLTs. (e),(f) Loop polarization rates. For all panels, the Fermi energy $E = 0.05$ and barrier width $d = 40a$ (a is the lattice constant).

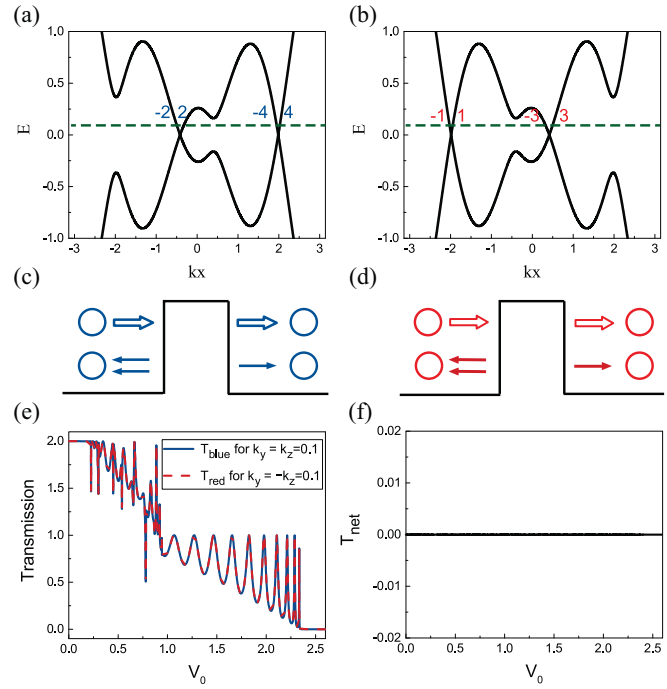

FIG. 3. Non-normal incidence of the linked case with $m_0 = 2.5$ and a rather large value of $k_z (= \pm k_y)$. (a),(b) Band structure cross sections in two loop planes: $k_y = k_z = 0.1$ and $k_y = -k_z = 0.1$, respectively, with Fermi energy $E = 0.05$ (dashed line). (c),(d) The corresponding scattering processes of (a) and (b). (e) Total transmissions T_{blue} and T_{red} for (a),(b), respectively. (f) The averaged NLT over (a) and (b).

the barrier boundaries, which are commonly seen in barrier tunnelings [35,37].

Next, we turn to the non-normal incidence of barrier tunneling, i.e., incident states at the Fermi surface with nonzero k_y and/or k_z. Since these two components, k_y and k_z, are conserved throughout the barrier tunneling, the scattering problem can still be reduced to the 1D cross section of the band structure $\mathcal{E}^{\pm}(k_x) \equiv E^{\pm}(k_x, k_y, k_z)$ with (k_y, k_z) fixed. For most pairs of fixed and finite (k_y, k_z), the band cross section $\mathcal{E}^{\pm}(k_x)$ will open a gap (therefore absence of the band-touching loop on this cross section) which may contain the Fermi energy if it is sufficiently large. As a result, these in-gap evanescent states will not contribute to measurable tunnelings. Since we are only interested in the low energy regime, only those states on the gapless cross sections $\mathcal{E}^{\pm}(k_x)$ should be considered. Here, we concentrate on the $k_y = k_z$ or $k_y = -k_z$ plane, where at least one loop exists. Without loss of generality, we take the linked case $m_0 = 2.5$ as an example.

In the $k_y = k_z = 0.1$ plane, states around the red loop open a gap but the blue ones remain, as illustrated in Fig. 3(a). In the $k_y = -k_z = 0.1$ plane at the same Fermi surface, the situation is just the reverse, as shown in Fig. 3(b). In the non-normal incidence, pseudospins of electrons are no longer conserved, because the term $\mathcal{A}$ in Hamiltonian (1) does not vanish. Thus, state '2' presented in Fig. 3(a), for example, can reflect back to '−2' and '−4,' shown in Fig. 3(c), while the corresponding processes are not allowed for the normal incidence. It is worthwhile to mention that the reflection from state '2' to state '−2' belongs to the highly unusual class of reflection called "electron retroreflection" [40,41], in which the electron's x directional and otherwise-directional group velocities simultaneously exhibit a sign reversal. This phenomenon appears commonly in nodal line semimetals [37] where velocities of states on the loop always point to or away from the loop center. By calculating transmissions, we find that the transmissions in the red and blue loops are completely identical, which lead to the vanishing of NLTs and loop polarizations, shown in Figs. 3(e) and 3(f). This unbiased result is because T_{red} and T_{blue} are contributed by two independent manifolds of states, respectively, along with the mirror symmetry of two loop planes

$$M_x H(k_z = k_y) M_x^{-1} = H(k_z = -k_y) \tag{6}$$

for a fixed k_y, where M_x is mirror operator reversing the sign of k_x. This symmetry even holds on for a small deviation δ from the loop plane in which the only loop opens a small gap,

$$M_x H(k_z = k_y + \delta) M_x^{-1} = H(k_z = -k_y - \delta) \tag{7}$$

for fixed k_y and δ.

The conclusion that loop polarization is mostly contributed from the vicinity of normal incidence is independent on the specific form of Hamiltonian (1) but relies on the mirror symmetry of two loop planes. The reason is as follows. The

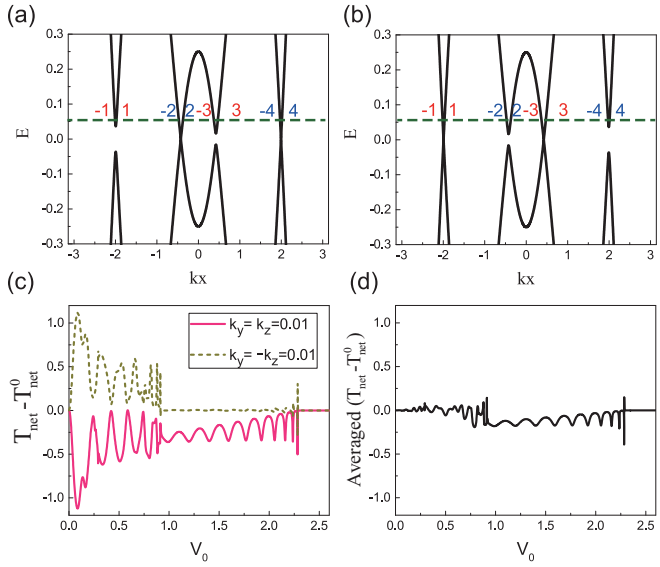

FIG. 4. Non-normal incidence in the linked case with $m_0 = 2.5$ and a sufficiently small value of $k_z(= \pm k_y)$. (a) and (b) are the band structure cross sections along k_x in two loop planes respectively: (a) $k_y = k_z = 0.01$ and (b) $k_y = -k_z = 0.01$, with Fermi energy $E = 0.05$ (dashed line). (c) NLTs for (a) (red solid) and (b) (yellow dashed) subtracted by T^0_{net}, the corresponding NLT at normal incidence [Fig. 2(c)]. (d) The average of two curves in (c).

loop states are all around the two loop planes $k_y = k_z$ and $k_y = -k_z$. As shown in Fig. 3, when the states are far away from the normal incidence with large value of $k_y = k_z$ and $k_y = -k_z$, electron states in the red and blue loops are scattered independently if the momenta are conserved in y and z directions. The scattering between two loops cannot happen. Thus, the loop polarization in this case is contributed by the two independent scattering processes of loops. If the mirror symmetry of two loop planes is conserved, the net loop transmission integrated over those electrons that are away from the normal incidence (i.e., with large value of $k_y = k_z$ and $k_y = -k_z$) on the Fermi surface is zero. This conclusion (the loop polarization is concentrated in the vicinity of normal incidence) is still valid if the deviation from the mirror symmetry is not large. The above discussion is about the injecting states with a rather large value of $k_z(= \pm k_y$ or $\pm(k_y + \delta))$ (δ is a tiny deviation), so that the 1D Fermi surface can only pass through either of the two loops, and the scattering is constrained in each loop.

Except for that, another typical case of non-normal incidence corresponds to injecting states completely on one loop plane and near the other loop plane, which corresponds to sufficiently small value of $k_z(= \pm k_y)$, with the band structure cross sections shown in Figs. 4(a) and 4(b). These band structures $\mathcal{E}^{\pm}(k_x)$ are very close to that of the normal incidence shown in Fig. 1(c), but there exists a tiny gap near one loop, respectively. Here, we still take the linked case $m_0 = 2.5$ as an example, with $k_y = \pm k_z = 0.01$ and the same Fermi energy $E = 0.05$ (dashed lines). Now the Fermi energy (dashed line) can pass through two loop regions, so that all four propagating channels are still active, and still, the conservation of pseudospin breaks.

We calculate the NLT from each loop plane, $T_{\text{net}}(k_y = k_z)$ and $T_{\text{net}}(k_y = -k_z)$. For comparison, we plot their differences from the normal incidence NLT $T^0_{\text{net}} \equiv T_{\text{net}}(k_y = k_z = 0)$ in Fig. 4(c). It seems that the differences are not ignorable. However, the average over two loop planes

$$T_{\text{net}} = \tfrac{1}{2}[T_{\text{net}}(k_y = k_z) + T_{\text{net}}(k_y = -k_z)] \tag{8}$$

is quite similar to T^0_{net}, which is manifested by their small difference represented in Fig. 4(d). In other words, the NLT from both loop planes at the same Fermi energy contribute complementarily, so that the total NLT is approximately equal to twice of that from normal incidence. The remaining small difference shown in Fig. 4(d) comes from possible mixed-loop scattering processes which were prohibited in the normal incidence due to pseudospin conservations.

Besides, the case with sufficiently small value of $k_z(= \pm(k_y + \delta))$ (δ is a small deviation) should also be considered to complete all possible cases of non-normal incidence. The physical picture is that injecting states are near both loop planes, near the normal incidence but on neither loop plane. Our numerical simulations indicate (but are not shown here) that the NLT is close to the result of the above case shown in Fig. 4, i.e., sufficiently small value of $k_z(= \pm(k_y))$.

Let us make a brief summary here. The normal incidence of barrier tunneling contributes to nonzero NLT (Fig. 2). For a non-normal incidence, if the incident state is far away from both two loop planes, the cross section of band structure along the x direction opens a full gap without any propagating state, contributing no transmission and no NLT. If the incident state is on (or very close to) one loop plane, but far away (large point-plane distance) from another loop plane, the transmissions of them are nonzero while the NLTs completely vanish (Fig. 3), due to the symmetric and independent transports of two loops. If the incident state is on (or close to) one loop plane and also close to (small point-plane distance) the other loop plane, the NLTs of them are close to the result of normal incidence (Fig. 4). In one word, the loop polarized transports in the Hopf semimetal only concentrate around the normal incidence. Incidence states far away from the normal one are either nonpolarized or nontransportable at all. Hence, the normal incidence contributes most of the NLT.

The above analysis is momentum $\boldsymbol{k}$ resolved. If we integrate over all momenta on the Fermi surface in the entire Brillouin zone, we can obtain the NLT and the loop polarization of the system. Although most states on the two loop planes do not contribute to NLT, but to conductance shown in Fig. 3, the loop polarization of the whole Hopf semimetal will not be completely submerged in the conductance after the momentum integration, since the total density of states (DOS) of a semimetal is very small around the loop energy ($E = 0$ for the present model), as will be explained in the following.

A more straightforward way for obtaining the full 3D information of loop polarization, in principle, is to simulate it in a quasi-1D bar shaped geometry (a quantum wire [39]) with a finite cross section (sufficiently large to make it "three-dimensional"). In the presence of barriers or disorders in the central region, the channel resolved scattering amplitudes on the Fermi energy can be numerically obtained directly [38,39]. However, it is now technically hard to

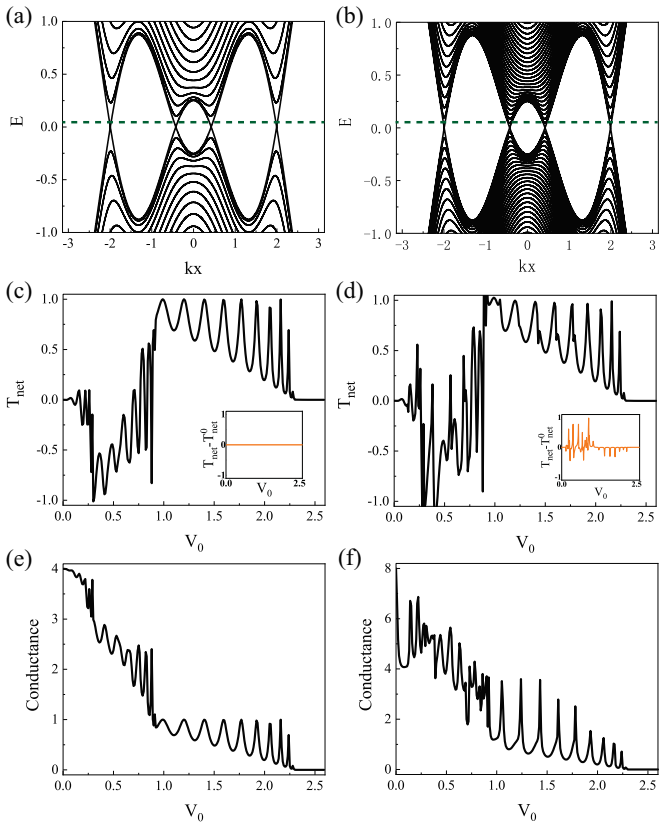

FIG. 5. (a),(b) Band structures along the x direction with $m_0 = 2.5$, $k_y = 0$, $N_z = 50a$ (left column), and $N_z = 120a$ (right column). The periodic boundary conditions is applied in the z direction. The horizontal dashed line represents the Fermi energy. (c),(d) NLTs as functions of barrier height V_0 corresponding to (a),(b). The insets show NLTs subtracted by T^0_{net} which is the corresponding NLT at normal incidence [Fig. 2(c)]. (e),(f) Conductances as functions of barrier height V_0 corresponding to (a),(b). For (c)–(f), the Fermi energy $E = 0.05$ and barrier width $d = 40a$ (a is the lattice constant).

distinguish channels (or subbands) on two different loops, when they are discretized due to the finite cross section. These quasi-1D subbands will distribute in an extremely complicated way, and those from two loops intertwine mutually and can hardly be distinguishable. In fact, this difficulty is rather fundamental. In graphene, the valleys are characterized by 0D Dirac points, and therefore they can be well distinguished even in the case of a quasi-1D ribbon [8]. In a 3D Hopf semimetal here, loops are closed 1D object embedded in a 2D or 3D space, and therefore they are barely distinguishable in a quasi-1D geometry (with other dimensions discretized).

Despite the above numerical difficulty, one can still go one step further, by calculating the scattering of the Hopf system with finite width N_z along the z direction while keeping N_y infinite (a slab geometry). Its loop scattering situations at $k_y = 0$ are shown in Fig. 5. It can be seen that when the Fermi energy is not large (i.e., near the loop zero energy), the total NLT of this slab just behaves like the normal incidence in the 3D limit [Fig. 2(c)]. For example, in Figs. 5(a), 5(c) and 5(e), we choose $N_z = 50a$ (a is the lattice constant) and there are only four right-propagating channels, identical to the normal incidence angle in Fig. 2. If we increase the width to

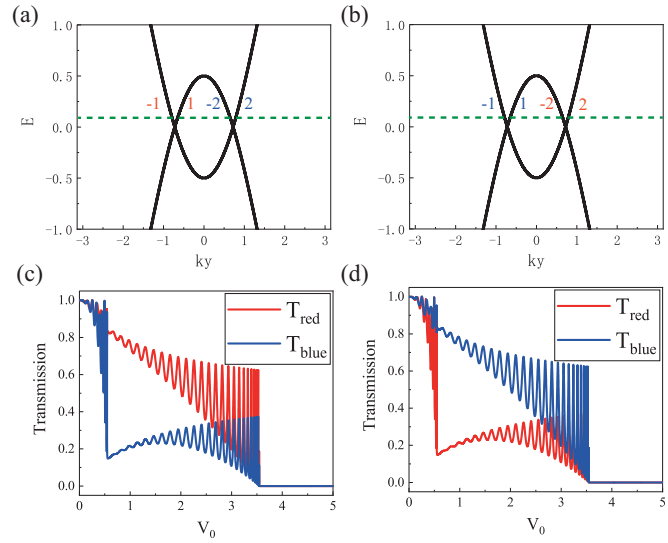

FIG. 6. (a),(b) Band structures along the y direction with $k_x = 0$, $k_z = 0.7227$, and $k_x = 0$, $k_z = -0.7227$, respectively. The horizontal dashed line represents the Fermi energy. (c),(d) Transmission amplitudes of electronic scattering into red (T_{red}) and blue (T_{blue}) loops corresponding to (a),(b), respectively, after tunneling into a barrier width. The Fermi energy $E = 0.05$ and the barrier width $d = 40a$ (a is the lattice constant).

$N_z = 120a$, as shown in Fig. 5(d), the total NLT is still close to the normal incidence in the 3D limit. Larger N_z may give rise to larger conductance, leading to a decrease of the loop polarization rate. However, this decrease is very slow, due to the small DOS of semimetals around zero energy. Note that if $k_y \neq 0$, most subbands along the x direction are gapped and therefore do not contribute to the total conductance. This is again the reminiscence of low DOS around the loop energy.

Therefore, the numerical results achievable so far are also useful and instructive for the understanding of the realistic loop transports. Due to the small DOS around zero, the electronic states at normal incidence play a significant role in the loop transports. For this reason, in the next section, the calculation of disorder induced loop polarization will be just based on the normal incidence.

So far, the transport direction is along the x direction, which connects the central points of two Hopf loops. In the case of conserving momentum in other two dimensions, this direction of transport offers the largest opportunities of interloop transition and therefore loop polarization, as can be seen from Fig. 1(a). For a comparison, let us take the transport direction to be the y direction, and the momenta k_x and k_z to be conserved. Similarly, this can be treated as an effectively 1D scattering problem along y, for a definite pair of (k_x, k_z), and scattering can only happen among states (k_x, k_y, k_z) on the Fermi surface (two loops). For most (k_x, k_z) in the BZ, the line ($k_x = \text{const}$, k_y, $k_z = \text{const}$) only crosses one loop and therefore the tunneling along this direction does not contribute to the loop polarization. Those (k_x, k_z) to make the line ($k_x = \text{const}$, k_y, $k_z = \text{const}$) cross both loops only consist of two very small windows. In Fig. 6, we plot the band structures and loop transports at the center of these two small windows, at Fermi energy $E = 0.05$. It is interesting to notice that the loop

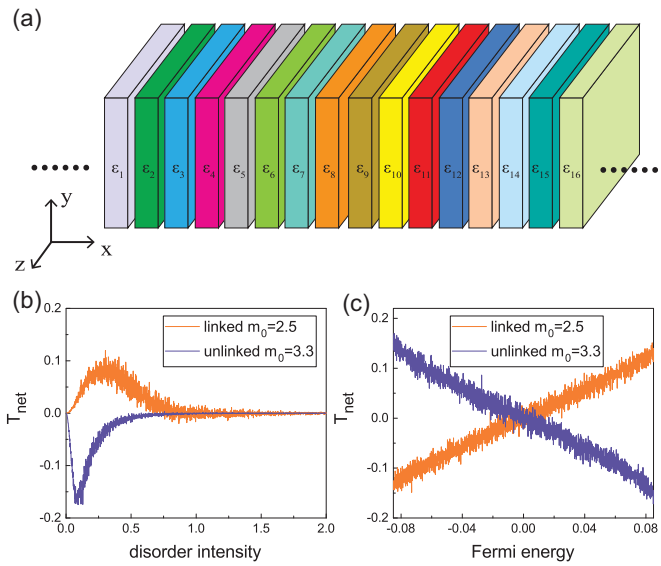

FIG. 7. (a) A schematic drawing of disorder distribution in real space, where different random numbers (ε_1, ε_2, ε_3,...) are shown on the slides with different colors and keep constant in y and z directions. (b) NLTs as functions of disorder intensity with Fermi energy $E = 0.05$. (c) NLTs as functions of Fermi energy with disorder intensity $W = 0.2$. In (b) and (c), the calculated values are averaged over 1000 disorder configurations. The scattering length $L = 40a$. The parameter $m_0 = 2.5$ (linked) for orange and $m_0 = 3.3$ (unlinked) for violet.

polarization through these two windows is perfectly *opposite*, which leads to no loop polarization. This is a result of the mirror symmetry along the z direction, i.e.,

$$M_z H(k_x = 0, k_z) M_z^{-1} = H(k_x = 0, -k_z). \tag{9}$$

Besides, states (k_x, k_z) away from these two windows of which only one loop or no loop exists also contribute to none of NLT, due to the product mirror symmetry

$$(M_x M_z) H(k_x, k_z)(M_x M_z)^{-1} = H(-k_x, -k_z). \tag{10}$$

The result of transporting along the z direction is similar. Moreover, the transport along other general axes can also be considered which is more complex and the loop polarization contribution from the broken symmetry needs to be introduced.

IV. DISORDER INDUCED LOOP POLARIZATION

To generalize the above results to a broader context, we relax the potential barrier (2) to a pseudospin independent random potential along the x direction:

$$V(\boldsymbol{x}) = V(x) = \begin{cases} \varepsilon_x, & 0 < x < d, \\ 0, & x < 0, x > d, \end{cases} \tag{11}$$

where ε_x are independent random numbers uniformly distributed in $(-W, W)$, with W the disorder intensity. Notice the potential ε_x is still y and z independent, but different on different x sheets, as shown in Fig. 7(a). Because ε_x is y and z independent, the scattering is still k_y and k_z conserving. As stated above, numerically, this setup makes us convenient to distinguish states in different loops which are still well fined in the $k_y - k_z$ plane. Furthermore, it is convenient to have a closer comparison with the k_y and k_z independent barrier in the last section. Here, we adopt 1000 configurations of random numbers to average the net loop transmission.

Such a disorder potential profile of sheets seems artificial, but the results will still be useful and representative, for reasons similar to those in last section. For example, the normal incidence still dominates the loop polarization, even if a finite width in one dimension is introduced, as depicted in Fig. 5. Even if the disorder potential breaks the translational symmetry in the y and z direction, so that the scattering between different momenta (k_y, k_z) is introduced, main conclusion in this section will not change.

Note that the pseudospin is still conserved at normal incidence in the presence of disorder defined in (11). Our calculations show that the loop polarizations are still centered around the normal incidence. Those electron states slightly deviated from normal incidence still behave like the normal incidence. Thus, in this section, the calculation of disorder-induced polarization is only focused on electronic states at normal incidence. Due to the strongly fluctuating potential from site to site, the NLT cannot have a simple picture of channel appearing or vanishing associated with the energy profile, as illustrated in Fig. 2.

In this case, a better way to understand disorder scattering is in the momentum space. Indeed, transmission or reflection amplitudes between states from disorder scattering are ultimately determined by the length of momentum transfer [8]. For the linked case shown in Figs. 1(c) and 1(e), the NLT can be attributed to the interloop reflection, in fact, mainly from the two shortest-momentum-transfer reflections '2'→'−3' and '3'→'−2,' which is confirmed in numerical calculations (not shown here). Due to the distinct distances of momentum transfer $|k_2^x - k_{-3}^x|$ and $|k_3^x - k_{-2}^x|$, the reflection from blue to red loop '2'→'−3' is much larger than the reflection from the red to blue loop '3'→'−2,' resulting in the polarization to the red loop. For the unlinked case shown in Figs. 1(d) and 1(f), on the other hand, the intraloop reflections of the red and blue loops are always identical, making no contribution to NLTs since their momentum transfer distances are the same, e.g., $|k_1^x - k_{-2}^x|$ ('1'→'−2') and $|k_3^x - k_{-4}^x|$ ('3'→'−4'). So does the interloop transmission, e.g., $|k_1^x - k_3^x|$ ('1'→'3') and $|k_2^x - k_4^x|$ ('2'→'4'). Thus, NLTs for the unlinked case can still be attributed to interloop reflection. The reflection from the red to blue loop '2'→'−3' is greater than the reflection from the blue to red loop '3'→'−2,' therefore leading to the polarization to the blue loop. This disorder induced loop polarization is similar to the valley polarization in graphene and other 2D materials [8].

We plot NLTs as functions of disorder intensity and as functions of Fermi energy in Figs. 7(b) and 7(c), respectively. In Fig. 7(b), the loop transmissions for the linked and unlinked cases polarize to opposite directions, since the relative positions of loop states are exchanged, e.g., '±2' ('±3') are the blue (red) loop states for the linked case, but red (blue) loop states for the unlinked case, shown in Figs. 1(c) and 1(d). As the disorder intensity continues to increase, NLTs reach the maxima, then drop to zero due to the Anderson localization. In Fig. 7(c), with the increase of the magnitude of

Fermi energy, NLTs become more remarkable, which can be explained by the increased differences of momentum transfer distance. Beside, as the Fermi energy goes to the negative value, the direction of polarization changes due to a jumping of shortest transfer momentum. For example, at a positive energy in Fig. 1(c), the momentum transfer of '2' → '−3' is shorter than that of '3' → '−2,' while at a negative energy the situation is reversed. Therefore a jumping between transfer processes occurs at $E = 0$.

The disorder-induced loop polarization only relies on the momentum transfer, which is completely similar to the disorder-induced valley polarization in two dimensions [8]. For the valley polarization, the intervalley backscattering has a valley contrasted rate due to momentum transfer difference between "from" and "to" processes of scattering, leading to a net transfer of population from one valley to another, after the transport along a certain direction. The relative positions between valleys determine the direction of polarization. Here, similarly, the relative positions of adjacent loop states play a crucial role in the transport in disordered systems. As a result, the direction of disorder-induced loop polarization is closely related to the topology: the linked or unlinked. Therefore, this loop polarization does not depend on other details of concrete models.

V. EFFECTS OF SMOOTH POTENTIAL BARRIER AND DISORDER

The infinitely sharp square potential barrier above might be difficult to achieve experimentally. A more realistic smooth potential profile has been considered in graphene [1]. Here, we adopt a Gaussian barrier frequently used in graphene models [8], written as

$$V(x) = V_0\left[\frac{1}{\sigma\sqrt{2\pi}}\exp\left(-\frac{(x-x_0)^2}{2\sigma^2}\right)\right], \qquad (12)$$

where x_0 is the center of barrier profile and σ characterizes the potential range. With the same reasons offered above, in this section, we only focus on the normal incidence, which plays the essential role in loop polarization.

The transmissions of incident loop states at normal incidence are shown in Figs. 8(a) and 8(b) with different σ. One can first notice that these transmission curves are smoother than those in the case of infinitely sharp potential barrier in Fig. 2(a). Comparing transmissions from different potential ranges in Figs. 8(a) and 8(b), two significant features can be seen: Larger σ gives rise to nearly perfect transmission plateaus, as well as larger differences in two loops which leads to more remarkable loop polarization as shown in Fig. 8(c). All these features can be well understood from the suppression of large momentum transfer from long range potential scattering [2,8,42], with the help of band structures illustrated in Fig. 1(c). In fact, with a larger potential range σ, the scattering with large $\Delta\boldsymbol{k}$, e.g., from state '1' to '±2,' '±3,' and '±4' will be more difficult to occur. As a result, the scattering will be more likely to be a "single valley" Dirac-like, i.e., a Klein tunneling without backscattering. This explains the almost perfect transmission plateaus at larger σ in Fig. 8(b). Then, similar to what happened in Fig. 2(a), due to different band structures (e.g., local energy cutoffs) around two loops,

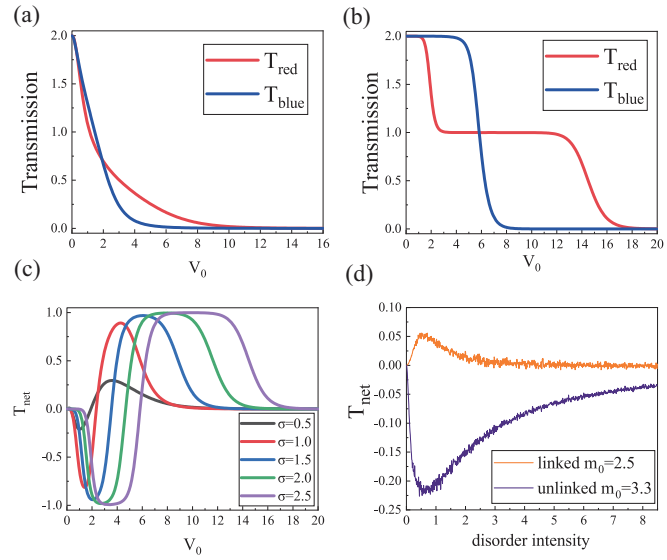

FIG. 8. (a), (b) Transmission amplitudes of electronic scattering into red (T_{red}) and blue (T_{blue}) loops with $\sigma = 0.5$ and $\sigma = 2.5$, respectively, as functions of the relative peak of Gaussian barrier V_0 in the case of $m_0 = 2.5$, $k_y = k_z = 0$. (c) NLTs as functions of the peak of Gaussian barrier V_0 with $\sigma = 0.5, 1.0, 1.5, 2.0, 2.5$. Other parameters are the same as (a),(b). (d) Disorder-induced loop polarizations as functions of the disorder intensity for linked $m_0 = 2.5$ and the unlinked $m_0 = 3.3$, with $k_y = k_z = 0$. The disorder profile is Gaussian with $\sigma = 0.5$ and the disorder density is 1%. The calculated disorder values are averaged over 5000 disorder configurations.

this transmission plateaus will vanish at different V_0 for two loops, leading to significant loop polarized transmission as a total. The scattering amplitudes for each channel are given in Appendix.

In this context, the disorder-induced loop polarization can also be discussed [8]. Gaussian disorders are written as

$$V(x) = \sum_{i=1}^{n_I}\left[\varepsilon_{x_i}\frac{1}{\sigma\sqrt{2\pi}}\exp\left(-\frac{(x-x_i)^2}{2\sigma^2}\right)\right], \qquad (13)$$

where ε_{x_i} are random numbers uniformly distributed in $(-W, W)$, with W the disorder intensity, representing the relative peak values of Gaussian impurities. x_i is the center position (also random) of the ith Gaussian impurity. The ratio $\rho_I = \frac{n_I}{N} \ll 1$ is defined to be the impurity density, where N is the total number of sites in the central region. The disorder-induced loop polarization is shown in Fig. 8(d), which is similar to that with infinitely sharp disorders in Fig. 7(b).

The loop dependent transmission plateaus through a smooth barrier shown in Fig. 8(b) can be used as a loop filter. We will show that it can also be used as a loop detector. Suppose a Hopf semimetal sample is connected to a two-terminal device, and this sample has a very finite cross section, so that those four groups (in four Dirac-like "valleys") of channels as shown in Fig. 1(c) dominate the quantum transport around the loop energy $E = 0$. Without loss of generality, we can suppose there is only one pair of channels in each group. In the absence of any barrier or disorder, the ballistic transmission T (which is just the conductance in units of $\frac{e^2}{h}$) is just 4, 2 for each loop. We can apply a back gate V_G around this

sample to introduce an effective potential barrier with long range smooth potential as described in Eq. (12). Increase the back gate V_G gradually until V_G^1 so that T drops to a stable value of 3. As can be seen from Fig. 8(b), this corresponds to an effective potential $V_0 \sim 4$, where the red loop has only one channel left.

Now if we inject a loop polarized current into this device, then their relative proportions (and therefore the polarization) can be obtained by using the following steps of measurements. First measure the conductance G_0 (which is proportional to the transmission T_0) without applying the gate voltage. Since all channels on both loops can ballistically transmit through the device without backscattering, we can write the total conductance as

$$G_0 = G_{\text{red}} + G_{\text{blue}}, \tag{14}$$

where the ratio between two terms reflects the proportions of two loops in the injecting current. After turning on the gate voltage to V_G^1, all blue loop channels will remain robust while half of the red loop channels will vanish [corresponding to $V_0 \sim 4$ in Fig. 8(b)], and therefore now the total conductance (also proportional to the transmission) should be

$$G_1 = G_{\text{red}}/2 + G_{\text{blue}}. \tag{15}$$

With measurable quantities G_0 and G_1, Eqs. (14) and (15), one can obtain the loop portions of the incoming current as

$$\begin{aligned} G_{\text{red}} &= 2(G_0 - G_1) \\ G_{\text{blue}} &= 2G_1 - G_0. \end{aligned} \tag{16}$$

Such finite-size point contact as a loop filter and detector is conceptually similar to that proposed for valleytronics in graphene [1]. Besides, if the spin-loop coupling is present, the loop current can be measured by detecting the spin current, similar to what was considered to valleytronics [8].

VI. SUMMARY

In this paper, we numerically study the quantum transport properties of Hopf semimetals based on a tight-binding model. We find that contributions of polarized transport are from the vicinity of normal incidence. The reason is as follows. For an incidence far away from normal, e.g., with large $k_y(= \pm k_z$ or $\pm(k_y + \delta))$, the NLT is completely canceled out after the average over two loop planes due to the mirror symmetry of two loop planes. For non-normal incidence with relatively small $k_y(= \pm k_z$ or $\pm(k_y + \delta))$, most transports of deviations from the normal incidence are eliminated as well. Due to the finite size effect along one direction, the electron states of Hopf semimetals at normal incidence play a dominant role in the quantum transport. Besides, smooth potential profiles can suppress the interloop scattering at normal incidence, resulting in the preservation of Klein tunneling.

At the normal incidence, restricted by the conversation of pseudospin, there exist two loop-scattering processes for linked and unlinked cases, respectively, indicating their different topologies. In the quantum transport through disordered regions, the opposite loop polarizations for the linked and unlinked cases also intrinsically reveals the topology.

A long range smooth potential barrier leads to strong suppression of large momentum transfer, and therefore gives rise to an even clearer picture of loop transports. For different potential heights, transmissions show almost perfect "on" (quantized) and "off" (zero) behaviors for different loops. This can be used as a controllable loop filter and detector. We expect that our findings can spur more researches on the realization of nodal line semimetals and the utilization of loop degree of freedom as a new carrier of information, i.e., looptronics.

ACKNOWLEDGMENTS

This work was supported by National Natural Science Foundation of China under Grants No. 11774336 and No. 61427901. Y.-Y.Z. was also supported by the Starting Research Fund from Guangzhou University under Grant No. RQ2020082.

APPENDIX

1. Mode matching approach

Our simulation method is mainly based on the algorithm developed by T. Ando, in a Green's function formalism [38,39]. Due to the Fisher-Lee relation [43–45], it is mathematically equivalent to the wave function approach, e.g., Kwant [46].

Consider a wire infinitely extending along the x direction with N degrees of freedom in a primitive cell or a "slide." The equation of motion can be written as

$$-\boldsymbol{H}_{01}^{\dagger}\boldsymbol{c}_{i-1} + (E\boldsymbol{I} - \boldsymbol{H}_{00})\boldsymbol{c}_i - \boldsymbol{H}_{01}\boldsymbol{c}_{i+1} = 0, \tag{A1}$$

where $\boldsymbol{H}_{00}$ is the Hamiltonian inside a slide and $\boldsymbol{H}_{01}$ is the hopping term between the nearest neighbor slides. $\boldsymbol{c}_i$ is the wave-function coefficient describing the amplitude at the position i. Then, we have the transfer matrix

$$\boldsymbol{T} = \begin{pmatrix} \boldsymbol{H}_{01}^{-1}(E\boldsymbol{I} - \boldsymbol{H}_{00}) & -\boldsymbol{H}_{01}^{-1}\boldsymbol{H}_{01}^{\dagger} \\ \boldsymbol{I} & \boldsymbol{0} \end{pmatrix}, \tag{A2}$$

which satisfies

$$\begin{pmatrix} \boldsymbol{c}_{i+1} \\ \boldsymbol{c}_i \end{pmatrix} = \boldsymbol{T}\begin{pmatrix} \boldsymbol{c}_i \\ \boldsymbol{c}_{i-1} \end{pmatrix}. \tag{A3}$$

Solve the equation below

$$\boldsymbol{T}\begin{pmatrix} \boldsymbol{c}_i \\ \boldsymbol{c}_{i-1} \end{pmatrix} = \lambda\begin{pmatrix} \boldsymbol{c}_i \\ \boldsymbol{c}_{i-1} \end{pmatrix}, \tag{A4}$$

and the $2N$ eigenvalues and $2N$ eigenvectors for $\boldsymbol{c}_i$ are obtained, which can be classified into N right- and N left-going channels. Let $\boldsymbol{U}(\pm) = (\boldsymbol{U}_1(\pm), ..., \boldsymbol{U}_N(\pm))$ be $\boldsymbol{c}_0$ of right and left-going solution corresponding to $(\lambda_1(\pm), ..., \lambda_N(\pm))$. The Fermi velocity corresponding to channel n is given by

$$v_n = -\frac{2}{\hbar} Im(\lambda_n \boldsymbol{U}_n^{\dagger}\boldsymbol{H}_{01}\boldsymbol{U}_n), \tag{A5}$$

where $\boldsymbol{U}_n$ is normalized here.

Let us define

$$\mathbf{\Lambda}(\pm) = \begin{pmatrix} \lambda_1(\pm) & & \\ & \ddots & \\ & & \lambda_N(\pm) \end{pmatrix}, \tag{A6}$$

and

$$\boldsymbol{F}(\pm) = \boldsymbol{U}(\pm)\Lambda(\pm)\boldsymbol{U}^{-1}(\pm), \tag{A7}$$

which satisfies

$$\boldsymbol{c}_i(\pm) = \boldsymbol{F}(\pm)^{i-i'}\boldsymbol{c}_{i'}(\pm). \tag{A8}$$

For the scattering problem, the infinite wire can be divided into three regions: left lead, scattering region, and right lead. After taking the effects of leads into account as self energies, the scattering matrix elements are found. For the incident channel ν with velocity v_ν and outgoing channel μ with velocity v_μ, the transmission coefficient is

$$t_{\mu\nu} = \sqrt{\frac{v_\mu}{v_\nu}}\{\boldsymbol{U}^{-1}(+)G_{N+1,0}\boldsymbol{H}_{01}^{\dagger}[\boldsymbol{F}^{-1}(+) - \boldsymbol{F}^{-1}(-)]\boldsymbol{U}(+)\}_{\mu\nu}, \tag{A9}$$

and the reflection coefficient is

$$r_{\mu\nu} = \sqrt{\frac{v_\mu}{v_\nu}}\{\boldsymbol{U}^{-1}(-)G_{0,0}\boldsymbol{H}_{01}^{\dagger}[\boldsymbol{F}^{-1}(+) - \boldsymbol{F}^{-1}(-) - 1]\boldsymbol{U}(+)\}_{\mu\nu}, \tag{A10}$$

where $G_{N+1,0}$ and $G_{0,0}$ are Green functions, which can be efficiently calculated by a slide-to-slide recursive method based on Dyson equation of Green's functions [47].

2. Scattering amplitudes of barrier tunneling at normal incidence

Here we show some details of channel resolved scattering amplitudes associated with the square barrier [Eq. (2)] and the smooth barrier [Eq. (12)]. The numeric label of each channel is defined in Figs. 1(c) and 1(d) for the linked and unlinked cases, respectively.

a. Square barrier

The scattering amplitudes through square barrier [Eq. (2)] tunneling at normal incidence for the linked case $m_0 = 2.5$ and the unlinked case $m_0 = 3.3$ are shown in Fig. 9 and Fig. 10, respectively. After a careful observation, it can be found that for both linked and unlinked cases, (1) state '1' can be transmitted into states '1,3' and reflected back to states '−2, −4;' (2) state '2' can be transmitted into states '2,4' and reflected back to states '−1, −3;' (3) state '3' can be transmitted into states '1,3' and reflected back to states '−2, −4;' (4) state '4' can be transmitted into states '2,4' and reflected back to states '−1, −3.' These phenomena are due to the pseudospin conservation, represented by the solid and dashed bands in Figs. 1(c) and 1(d). Also notice that for the linked case in Fig. 1(c), states '−1, 1, −3, 3' belong to the red loop while states '−2, 2, −4, 4' belong to the blue loop, while for the unlinked case in Fig. 1(d), states '−1, 1, −2, 2' belong to the red loop while states '−3, 3, −4, 4' belong to the blue loop. Hence, the conclusions in Figs. 1(e) and 1(f) and the numerical results in Fig. 2 can be obtained straightforwardly after a classification of "red" and "blue" loop states.

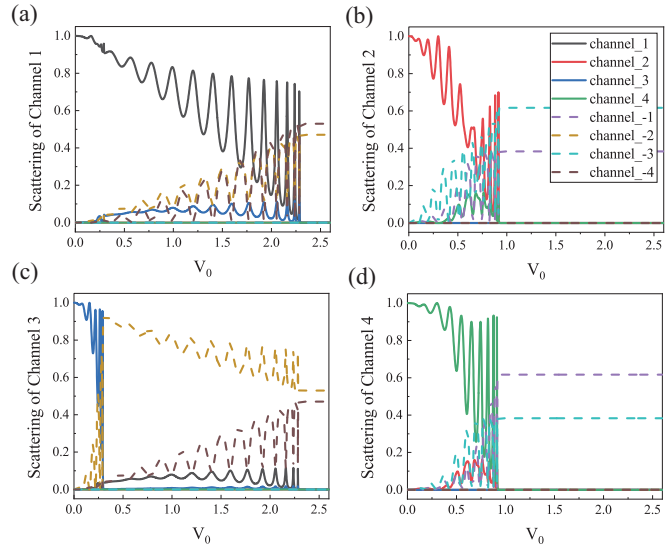

FIG. 9. Scattering amplitudes of barrier tunneling at normal incidence for the linked case $m_0 = 2.5$, corresponding to Figs. 2(a), 2(c) and 2(e). (a)–(d) are the scattering of the incident states '1,2,3,4,' respectively. The numeric labels '1,2,3,4' and '−1, −2, −3, −4' for channels are shown in Fig. 1(c). The solid lines represent the transmission results and the dashed lines represent the reflection results. All the subfigures share the same legend.

b. Smooth barrier

The scattering amplitudes of smooth barrier [Eq. (12)] tunneling at normal incidence for the linked case $m_0 = 2.5$ with the potential range $\sigma = 0.5$ and $\sigma = 2.5$ are shown in Figs. 11 and 12, respectively. The pseudospin conservation still influences the scattering processes here. For example,

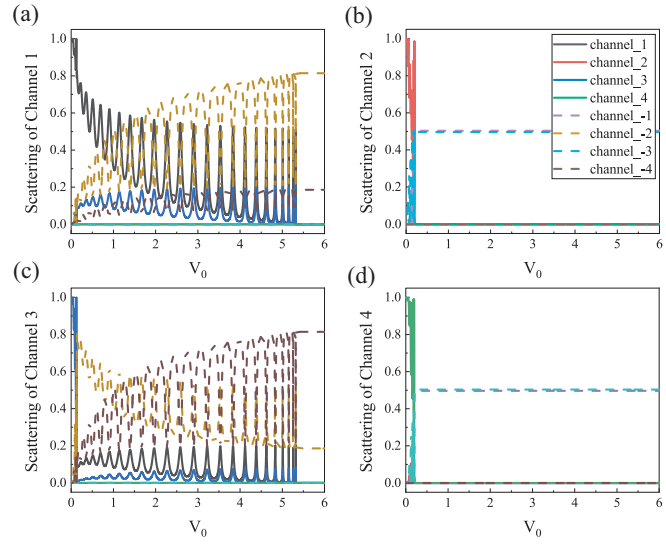

FIG. 10. Scattering amplitudes of barrier tunneling at normal incidence for the unlinked case $m_0 = 3.3$, corresponding to Figs. 2(b), 2(d) and 2(f). (a)–(d) are the scattering of the incident states '1,2,3,4,' respectively. The numeric labels '1,2,3,4' and '−1, −2, −3, −4' for channels are shown in Fig. 1(d). Other notations are the same as Fig. 9.

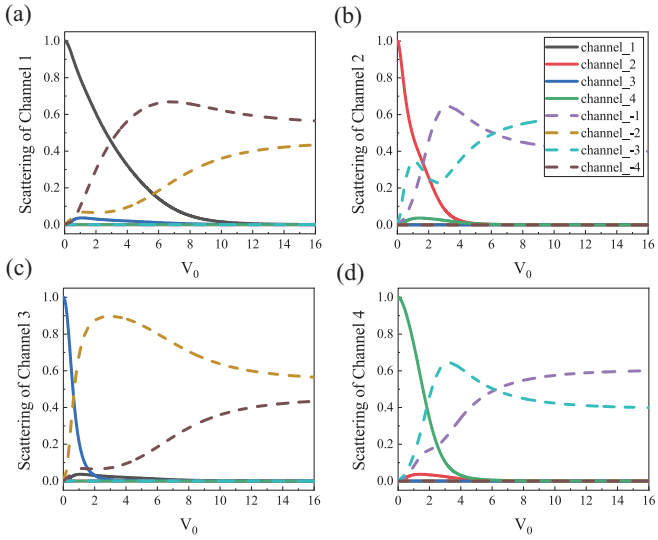

FIG. 11. Similar to Fig. 9 but for a smooth barrier $\sigma = 0.5$, corresponding to Fig. 8(a).

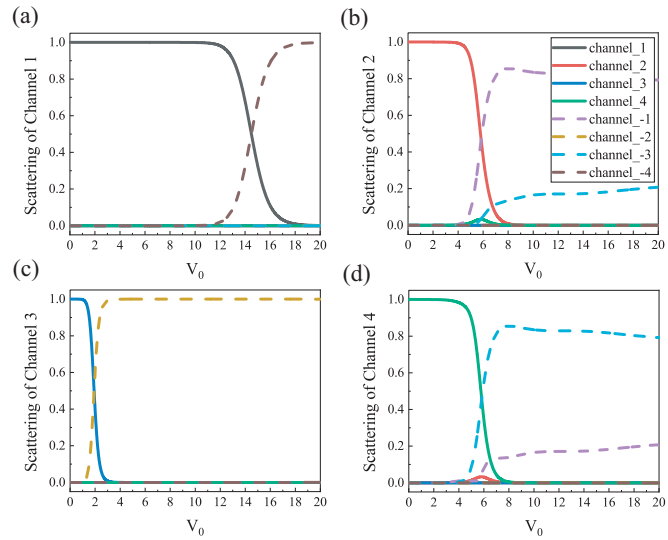

FIG. 12. Similar to Fig. 9 but for a smooth barrier with a larger $\sigma = 2.5$, corresponding to Fig. 8(b).

state '1' can only be transmitted into states '1,3' and reflected back to states '$-2, -4$.' We can find that the curves of the scattering amplitudes in Fig. 11 and Fig. 12 are smoother than those for infinitely sharp potential barrier in Fig. 9. For a larger σ, i.e., $\sigma = 2.5$ in Fig. 12, the Klein tunneling with perfect transmission maintains even for enough large V_0, because of the suppression of large momentum transfer (i.e., effective prohibition of inter-"valley" scattering which is far in the momentum space). Note that for the linked case, states in channels '1,3' belong to the red loop and states in channels '2,4' belong to the blue loop. Due to the band structures in Fig. 1(c), the transmission plateaus of red and blue loops drop down at different V_0, leading to the loop polarized transmissions, shown in Figs. 8(a)–8(c).

[1] A. Rycerz, J. Tworzydło, and C. W. J. Beenakker, Valley filter and valley valve in graphene, Nat. Phys. **3**, 172 (2007).

[2] D. Xiao, W. Yao, and Q. Niu, Valley-Contrasting Physics in Graphene: Magnetic Moment and Topological Transport, Phys. Rev. Lett. **99**, 236809 (2007).

[3] F. Zhai and K. Chang, Valley filtering in graphene with a Dirac gap, Phys. Rev. B **85**, 155415 (2012).

[4] D. Gunlycke and C. T. White, Graphene Valley Filter Using a Line Defect, Phys. Rev. Lett. **106**, 136806 (2011).

[5] M. Sui, G. Chen, L. Ma, W.-Yu. Shan, D. Tian, K. Watanabe, T. Taniguchi, X. Jin, W. Yao, D. Xiao, and Y. Zhang, Gate-tunable topological valley transport in bilayer graphene, Nat. Phys. **11**, 1027 (2015).

[6] Y. Shimazaki, M. Yamamoto, I. V. Borzenets, K. Watanabe, T. Taniguchi, and S. Tarucha, Generation and detection of pure valley current by electrically induced Berry curvature in bilayer graphene, Nat. Phys. **11**, 1032 (2015).

[7] K. Takashina, Y. Ono, A. Fujiwara, Y. Takahashi, and Y. Hirayama, Valley Polarization in Si(100) at Zero Magnetic Field, Phys. Rev. Lett. **96**, 236801 (2006).

[8] X.-T. An, J. Xiao, M. W.-Y. Tu, H. Yu, V. I. Fal'ko, and W. Yao, Realization of Valley and Spin Pumps by Scattering at Nonmagnetic Disorders, Phys. Rev. Lett. **118**, 096602 (2017).

[9] K. F. Mak, K. He, J. Shan, and T. F. Heinz, Control of valley polarization in monolayer MoS_2 by optical helicity, Nat. Nanotechnol. **7**, 494 (2007).

[10] D. Xiao, G.-B. Liu, W. Feng, X. Xu, and W. Yao, Coupled Spin and Valley Physics in Monolayers of MoS_2 and other Group-VI Dichalcogenides, Phys. Rev. Lett. **108**, 196802 (2012).

[11] H. Zeng, J. Dai, W. Yao, D. Xiao, and X. Cui, Valley polarization in MoS_2 monolayers by optical pumping, Nat. Nanotechnol. **7**, 490 (2007).

[12] K. F. Mak, K. L. McGill, J. Park, and P. L. McEuen, The valley Hall effect in MoS_2 transistors, Science **344**, 1489 (2014).

[13] A. A. Burkov, M. D. Hook, and L. Balents, Topological nodal semimetals, Phys. Rev. B **84**, 235126 (2011).

[14] C. Fang, H. Weng, X. Dai, and Z. Fang, Topological nodal line semimetals, Chi. Phys. B **25**, 117106 (2016).

[15] P.-Y. Chang and C.-H. Yee, Weyl-link semimetals, Phys. Rev. B **96**, 081114 (2017).

[16] Z. Yan, R. Bi, H. Shen, L. Lu, S.-C. Zhang, and Z. Wang, Nodal-link semimetals, Phys. Rev. B **96**, 041103 (2017).

[17] G. Chang, S.-Y. Xu, X. Zhou, S.-M. Huang, B. Singh, B. Wang, I. Belopolski, J. Yin, S. Zhang, A. Bansil, H. Lin, and M. Z. Hasan, Topological Hopf and Chain Link Semimetal States and Their Application to Co_2MnGa, Phys. Rev. Lett. **119**, 156401 (2017).

[18] W. Chen, H.-Z. Lu, and J.-M. Hou, Topological semimetals with a double-helix nodal link, Phys. Rev. B **96**, 041102 (2017).

[19] Y. Zhou, F. Xiong, X. Wan, and J. An, Hopf-link topological nodal-loop semimetals, Phys. Rev. B **97**, 155140 (2018).

[20] X. Tan, M. Li, D. Li, K. Dai, H. Yu, and Y. Yu, Demonstration of Hopf-link semimetal bands with superconducting circuits, Appl. Phys. Lett. **112**, 172601 (2018).

[21] L. Li, S. Chesi, C. Yin, and S. Chen, 2π-flux loop semimetals, Phys. Rev. B **96**, 081116 (2017).

[22] J. Cai, Y. Xie, P.-Y. Chang, H.-S. Kim, and Y. Chen, Nodal-chain network, intersecting nodal rings and triple points coexisting in nonsymmorphic Ba_3Si_4, Phys. Chem. Chem. Phys. **20**, 21177 (2018).

[23] Q. Yan, R. Liu, Z. Yan, B. Liu, H. Chen, Z. Wang, and L. Lu, Experimental discovery of nodal chains, Nat. Phys. **14**, 461 (2018).

[24] T. Bzdušek, Q. Wu, A. Rüegg, M. Sigrist, and A. A. Soluyanov, Nodal-chain metals, Nature (London) **538**, 75 (2016).

[25] X. Feng, C. Yue, Z. Song, Q. Wu, and B. Wen, Topological Dirac nodal-net fermions in AlB_2-type TiB_2 and ZrB_2, Phys. Rev. Materials **2**, 014202 (2018).

[26] C. Gong, Y. Xie, Y. Chen, H.-S. Kim, and D. Vanderbilt, Symmorphic Intersecting Nodal Rings in Semiconducting Layers, Phys. Rev. Lett. **120**, 106403 (2018).

[27] R. Bi, Z. Yan, L. Lu, and Z. Wang, Nodal-knot semimetals, Phys. Rev. B **96**, 201305 (2017).

[28] M. Ezawa, Topological semimetals carrying arbitrary Hopf numbers: Fermi surface topologies of a Hopf link, Solomon's knot, trefoil knot, and other linked nodal varieties, Phys. Rev. B **96**, 041202 (2017).

[29] J. Lian, L. Yu, Q.-F. Liang, J. Zhou, R. Yu, and H. Weng, Multi-loop node line states in ternary MgSrSi-type crystals, npj Computational Materials **5**, 10 (2019).

[30] C.-K. Chiu and A. P. Schnyder, Classification of reflection-symmetry-protected topological semimetals and nodal superconductors, Phys. Rev. B **90**, 205136 (2014).

[31] Y. Liu, J. Song, Y. Li, Y. Liu, and Q.-F. Sun, Controllable valley polarization using graphene multiple topological line defects, Phys. Rev. B **87**, 195445 (2013).

[32] Y. S. Ang, S. A. Yang, C. Zhang, Z. Ma, and L. K. Ang, Valleytronics in merging Dirac cones: All-electric-controlled valley filter, valve, and universal reversible logic gate, Phys. Rev. B **96**, 245410 (2017).

[33] F. Wilczek and A. Zee, Linking Numbers, Spin, and Statistics of Solitons, Phys. Rev. Lett. **51**, 2250 (1983).

[34] O. Klein, Die reflexion von elektronen an einem potentialsprung nach der relativistischen dynamik von dirac, Zeitschrift für Physik **53**, 157 (1929).

[35] M. I. Katsnelson, K. S. Novoselov, and A. K. Geim, Chiral tunneling and the Klein paradox in graphene, Nat. Phys. **2**, 620 (2006).

[36] R. D. Y. Hills, A. Kusmartseva, and F. V. Kusmartsev, Current-voltage characteristics of Weyl semimetal semiconducting devices, Veselago lenses, and hyperbolic Dirac phase, Phys. Rev. B **95**, 214103 (2017).

[37] J.-H. Guan, Y.-Y. Zhang, W.-E. Lu, Y. Xia, and S.-S. Li, Barrier tunneling of the loop-nodal semimetal in the hyperhoneycomb lattice, J. Phys.: Condens. Matter **30**, 185402 (2018).

[38] T. Ando, Quantum point contacts in magnetic fields, Phys. Rev. B **44**, 8017 (1991).

[39] P. A. Khomyakov, G. Brocks, V. Karpan, M. Zwierzycki, and P. J. Kelly, Conductance calculations for quantum wires and interfaces: Mode matching and Green's functions, Phys. Rev. B **72**, 035450 (2005).

[40] Y. S. Ang, Z. Ma, and C. Zhang, Retro reflection of electrons at the interface of bilayer graphene and superconductor, Sci. Rep. **2**, 1013 (2006).

[41] B. Lv and Z. Ma, Electronic equivalence of optical negative refraction and retroreflection in the two-dimensional systems with inhomogeneous spin-orbit couplings, Phys. Rev. B **87**, 045305 (2013).

[42] R. Logemann, K. J. A. Reijnders, T. Tudorovskiy, M. I. Katsnelson, and S. Yuan, Modeling Klein tunneling and caustics of electron waves in graphene, Phys. Rev. B **91**, 045420 (2015).

[43] D. S. Fisher and P. A. Lee, Relation between conductivity and transmission matrix, Phys. Rev. B **23**, 6851 (1981).

[44] S.-H. Zhang, W. Yang, and K. Chang, General Green's function formalism for layered systems: Wave function approach, Phys. Rev. B **95**, 075421 (2017).

[45] H. Boumrar, M. Hamidi, H. Zenia, and S. Lounis, Equivalence of wave function matching and Green's functions methods for quantum transport: generalized Fisher-Lee relation, J. Phys.: Condens. Matter **32**, 355302 (2020).

[46] C. W. Groth, M. Wimmer, A. R Akhmerov, and X. Waintal, Kwant: a software package for quantum transport, New J. Phys. **16**, 063065 (2014).

[47] A. MacKinnon, The calculation of transport properties and density of states of disordered solids, Z. Phys. B: Condens. Matter **59**, 385 (1985).